



# Electronic metal-support interaction via defective-induced platinum modified BiOBr for photocatalytic N<sub>2</sub> fixation



Guangmin Ren <sup>a</sup>, Meng Shi <sup>a</sup>, Zizhen Li <sup>a</sup>, Zisheng Zhang <sup>b</sup>, Xiangchao Meng <sup>a,\*</sup>

<sup>a</sup> Key Laboratory of Marine Chemistry Theory and Technology, Ministry of Education, College of Chemistry and Chemical Engineering, Ocean University of China, Qingdao 266100, China

<sup>b</sup> Department of Chemical and Biological Engineering, Faculty of Engineering, University of Ottawa, Ottawa, Ontario K1N6N5, Canada

## ARTICLE INFO

**Keywords:**  
 Photocatalytic  
 EMSI effect  
 Active sites  
 Oxygen vacancy  
 Density functional theory  
 N<sub>2</sub> fixation

## ABSTRACT

Designing atomic-scale catalytic sites to facilitate N<sub>2</sub> adsorption and transport of photogenerated electrons to the target active sites offers new opportunities to achieve highly-efficiently photocatalytic N<sub>2</sub> reduction reactions. Herein, Pt was photodeposited on BiOBr along with formation of oxygen vacancies (OVs) under ultraviolet light. The modulation of chemical states of Pt and the formation of electron metal-support interactions (EMSI) between BOB and Pt facilitated the charge transfer between the modifiers (i.e. Pt and OVs) and the support (i.e. BiOBr). The production rate of ammonia on Pt and OVs co-modified BiOBr reached 23.8 μmol g<sup>-1</sup> h<sup>-1</sup>, which was much higher than that either on OVs-BiOBr or pristine BiOBr. Density functional theory (DFT) calculations showed that EMSI effect led to a significant charge redistribution between Pt and BOB carriers, whereby Pt doping could significantly reduce energy barrier of N<sub>2</sub> hydrogenation process to facilitate photocatalytic N<sub>2</sub> reduction.

## 1. Introduction

Ammonia is an important product in various fields, especially for the production of artificial fertilizers [1–3]. Nowadays, industrial ammonia is still primarily produced by Harsh-Bosch process which was invented at the beginning of the 1900 s. This process consumes huge amounts of fossil resources and emits large amounts of greenhouse gases such as CO<sub>2</sub> [4–6]. Photocatalytic nitrogen reduction reaction (NRR) triggered by renewable solar energy holds great promise as a safe, low-cost, environmentally-friendly and sustainable route to synthesize ammonia.

Many conventional photocatalysts including metal-containing materials (e.g. metal oxides [7,8], metal sulfides [9]) and metal-free materials (e.g. Graphene Oxide [10], carbon nitride [11,12]) have been investigated for N<sub>2</sub> reduction. However, the highly selective ammonia synthesis reaction via N<sub>2</sub> and water (i.e. converting N<sub>2</sub> and H<sub>2</sub>O to ammonia without sacrificial agents) remains a challenge for photocatalysis. The strong N≡N triple bonds are refractory to activate and cleave [3,13–15]. Additionally, the hydrogenation of activated nitrogen molecules represents one of the nonnegligible rate-determining steps [8, 16]. Thus, multi-electron reduction process of photocatalytic conversion of N<sub>2</sub> and H<sub>2</sub>O establishes a high standard for the design of efficient photocatalysts: i) the active sites should be able to accumulate a

substantial amount of photogenerated electrons to facilitate N<sub>2</sub> activation; ii) the hydrogenation step of adsorbed nitrogen (\*N<sub>2</sub>) can be enhanced by tuning the electronic structure of the catalyst or by surface modification. Therefore, selecting suitable semiconductor with sufficient reactive sites is crucial to achieve highly efficient photocatalytic synthesis of ammonia [11,17–19].

BiOBr (BOB) is an attractive candidate for photocatalytic NRR owing to its narrow band gap, controllable structure and high chemical stability [20,21]. Nevertheless, the main limitation of N<sub>2</sub> photoreduction results from the weak interaction between N<sub>2</sub> and BOB, which makes it difficult to activate inert N≡N bonds. In addition, the faster recombination of photogenerated electrons and holes kinetically limits photocatalytic activity in N<sub>2</sub> reduction of BOB [22]. Recently, various single atoms have proven to be promising for ammonia synthesis due to particular electronic structures and atomically dispersed active sites, including Fe [23], Cu [24,25], Ru [26] and other metal heteroatom dopants. Electronic metal-support interaction (EMSI) is considered as an effective approach to modulate the electronic structure and accelerate the transfer of charge carriers with formation a channel [27,28]. Commonly, EMSI was widely applied to effectively stabilize single-atom catalysts (SACs), which would provide a higher oxidation state to the active site through electron transfer between the single atom and the

\* Corresponding author.

E-mail address: mengxiangchao@ouc.edu.cn (X. Meng).

support [28,29]. A strong EMSI would provide a flexible electron environment and accelerate electrons' transfer, which would promote the selective adsorption of reactants, thus reducing the energy barrier and facilitating the rate-limiting step [27,30–32]. Oxygen vacancies [33] were easily produced on BOB by ultraviolet light illumination, which can induce the deposition of metallic compounds and fabrication of EMSI. Therefore, BOB can be applied as a good support for EMSI, but it has been rarely reported to improve the photocatalytic activity of BOB in NRR.

Herein, we have developed a simple photodeposition method to fabricate Pt/BOB with finely tunable oxidation state of Pt single atom by controlling the synthesis conditions. With the modulation of the chemical states of Pt and the formation of EMSI between BOB and Pt, the photocatalytic activity and selectivity have been greatly improved in NRR for ammonia synthesis. Based on in-situ characterizations and density functional theory (DFT) calculations, it revealed that EMSI promotes the transfer of electrons from BOB atoms to Pt, enhancing the adsorption and activation of N<sub>2</sub>. By tuning the local electron structure of the oxygen vacancy by Pt doping, the local electron density of the adsorbed N<sub>2</sub> can be adjusted, further promoting the hydrogenation of \*N<sub>2</sub> as well as lowering the energy barrier of the rate-limiting step. This work provides new insights in controlling the surface catalytic sites at the atomic scale to optimize the reaction pathways in the multi-electron N<sub>2</sub> photoreduction process.

## 2. Experimental section

### 2.1. Chemicals

Chloroplatinic acid hydrate (H<sub>2</sub>PtCl<sub>6</sub>·6H<sub>2</sub>O, AR) was purchased from Sigma-Aldrich and used without further purification. Bismuth nitrate pentahydrate (Bi(NO<sub>3</sub>)<sub>3</sub>·5H<sub>2</sub>O), and potassium bromide (KBr) were ordered from Sinopharm Chemical Reagent Co. Ltd. and used for preparing catalysts. Nafion was purchased from Aladdin Ltd. (Shanghai, China). Ultrapure water used throughout all experiments was purified through a Millipore system.

### 2.2. Materials synthesis

**Preparation of BOB catalysts:** Typically, 0.485 g of Bi(NO<sub>3</sub>)<sub>3</sub>·5 H<sub>2</sub>O was separately dissolved in 15-mL deionized (DI) water, stirring continuously until well dispersed. Then, 15 mL of DI water containing 0.119 g of KBr was dropwise added into above solution. Subsequently, after stirring for 30 min, the suspension was stirred for 30 min and transferred to a 50-mL Teflon-lined stainless-steel autoclave (Anhui CHEMN Instrument Co., Ltd., HT-100 H-316 L), heated up to 160 °C and maintained for 24 h. After naturally cooling down to room temperature, the obtained powder was collected by centrifugation, washed thoroughly with DI water and ethanol, and dried at 80 °C in a vacuum oven overnight.

**Preparation of the Pt<sub>x</sub>/BOB-V<sub>O</sub> catalysts:** BOB (0.50 g) was first dispersed in 100-mL DI water, followed by ultrasonication for 30 min. Before illumination, the suspensions were bubbled with high-purity O<sub>2</sub> (99.999%) continuously for 30 min in dark under stirring. Pt precursor (H<sub>2</sub>PtCl<sub>6</sub>·6 H<sub>2</sub>O) was then added under the irradiation of a 300-W Hg lamp for 30 min while bubbling high-purity O<sub>2</sub> through the suspension at flow rate of 30 mL/min. The final products were placed in an oven and dried at 60 °C for 12 h for further use. The products were named x wt% M/BOB-V<sub>O</sub> (M = Pt, Pd, Au, Ru, Ag and x = 0, 0.25, 0.50, 0.75, 1.0), where x means the mass percentage of the doped metal elements. Among them, the samples are defined as Pt<sub>x</sub>/BOB-V<sub>O</sub>, where Pt value is 0.50 wt %. For comparison, 0.50 wt% Pt/BOB-V<sub>O</sub> (A) with various gas atmospheres (N<sub>2</sub>, Air, Ar) was also prepared under the same condition.

### 2.3. Characterizations

X-ray diffraction (XRD) patterns were collected on a Rigaku RINT 2500 TTRAX-III with Cu K $\alpha$  radiation. Further morphologies and chemical composition analyses were performed using a Hitachi S-4800 field emission scanning electron microscope (SEM) equipped with energy-dispersive spectroscopy (EDS) images. Transmission electron microscopy (TEM), high-resolution TEM (HRTEM) using a JEOL 2100 F instrument at an accelerating voltage of 200 kV. A JEM-ARM200F TEM/STEM with a spherical aberration corrector working at 300 kV recorded the high angle annular dark-field scanning transmission electron microscopy (HAADF-STEM). Ultraviolet-visible (UV-vis) diffuse reflectance spectroscopy (DRS) were acquired on a PUXI TU-1901 spectrometer. Photoluminescence spectra were obtained at room temperature using a fluorescence spectrophotometer (Thermo ESCALAB 250XI). Electron paramagnetic resonance (EPR) spectra were obtained on a Bruker EMX-8/2.7 C at 100 K. Nitrogen adsorption-desorption isotherms were obtained at 77 K using the AUTOSORB IQ. Temperature programmed desorption of N<sub>2</sub> (N<sub>2</sub>-TPD) measurements were performed in a quartz reactor with a TCD detector. X-ray photoelectron spectroscopy (XPS) data were taken on a Thermo Scientific K-Alpha X-ray photo-electron spectrometer with monochromatized Al-K $\alpha$  ( $\hbar\nu$  = 1486.60 eV). The samples were analyzed for metal content using a Perkin Elmer optima 8300 inductively coupled plasma optical emission spectrometry (ICP-OES). Time-resolved photoluminescence (TR-PL) spectra were recorded on a Jobin Yvon Horiba Fluorolog-3-Tau Spectrofluorometer.

### 2.4. Photoreduction of N<sub>2</sub>

The photocatalytic NRR performance of the photocatalysts was evaluated under a 300-W Xe lamp (PLS-FX300HU, Beijing Perfect light Co. Ltd.) with a light intensity of 491 mW cm<sup>-2</sup> as the light source. In a typical experiment, 30 mg of photocatalyst was dispersed in 60 mL of distilled water with N<sub>2</sub> (purity > 99.999%) bubbling for 30 min in a quartz reactor without oxygen contaminants. As an important guarantee, N<sub>2</sub> was passed through a gas wash bottle containing dilute sulfuric acid and water before being introduced into the quartz reactor to remove any possible N contaminants. The reactor was then irradiated under a 300-W Xe lamp and equipped with a circulating water outer jacket to maintain a constant temperature of 25 °C. At regular intervals, 10 mL aliquot of the reaction solution was collected using a syringe and then filtrated through a 0.22 μm filter to remove the residual catalysts. Moreover, the concentration of produced NH<sub>4</sub><sup>+</sup> was determined by colorimetry (Nessler's reagent method) and ion chromatography (ICS-1100). The concentration-absorbance curve was calibrated using a standard ammonia solution with a series of concentrations (Fig. S1). The fitting curve ( $y = 0.1123 x - 0.0027$ ,  $R^2 = 0.999$ ) showed good linear relation of absorbance value with ammonia concentration. Meanwhile, a standard curve of ammonia by ion chromatography was presented in Fig. S2. The calibration curve ( $y = 0.2286 x - 0.0019$ ,  $R^2 = 0.999$ ) was plotted from peak area versus the concentration of ammonia. The content of N<sub>2</sub>H<sub>4</sub> was determined by the Watt and Chrissp method (Fig. S3). UV-Vis absorption spectra of the colored complexes formed in the colorimetric tests were collected on a TU-1901 spectrophotometer. The fitting curve showed good linear relation of absorbance with N<sub>2</sub>H<sub>4</sub> concentration ( $y = 0.588 x + 0.027$ ,  $R^2 = 0.999$ ).

Apparent quantum efficiency (AQE) was further determined. Specifically, 30 mg of Pt<sub>x</sub>/BiOBr-V<sub>O</sub> was dispersed in 60 mL DI water. To obtain the AQE, the reaction solution was irradiated by a 300 W Xe lamp with different wavelength band-pass filters (365, 400, 500, 600, and 700 nm). The photon flux of the incident light was measured by a light power meter (CEL-NP2000-2(10)A, China). The AQE was calculated according to Eq. 1 as below [34,35]:

$$\text{AQE} = \frac{\text{Number of reacted electrons}}{\text{Number of incident photons}} \times 100\% = \frac{3 \cdot n_{AM} \cdot N_A}{\frac{W \cdot A \cdot t}{h \nu}} \times 100\% \quad (1)$$

where  $n_{AM}$ , W, A, t and  $\nu$  represent the molar number of generated ammonia, the incident light intensity, irradiation area, time and frequency, respectively;  $N_A$  and h is the Avogadro's constant and Planck constant, respectively.

## 2.5. Electrochemical tests

The electrochemical measurements were performed on a CHI 660E electrochemical workstation equipped with a three-electrode cell. The working electrode was a glassy carbon electrode coated with catalyst, the counter electrode was a platinum foil, and the reference electrode was a saturated Ag/AgCl electrode. Typically, 5 mg photocatalysts and 20  $\mu\text{L}$  of Nafion solution were evenly dispersed in 200  $\mu\text{L}$  of deionized water, then 40  $\mu\text{L}$  of the solution was dip-coated on a  $1 \times 1 \text{ cm}^2$  FTO glass and then dried at room temperature. Electrochemical impedance spectroscopy (EIS) measurements and the transient photocurrent responses of different samples were conducted in 0.5 M  $\text{Na}_2\text{SO}_4$  aqueous solution.

## 3. Results and discussion

### 3.1. Preparation and characterizations

As illustrated in Fig. 1a, Pt-doped BiOBr with oxygen vacancies were

prepared by a hydrothermal method followed by a photodeposition strategy. Initially, BiOBr nanosheets were synthesized using a mild hydrothermal method. Further, the unsaturated vacancies as the strong anchor sites of metals were known formed by UV light activation. The Pt-doped BOB nanosheets were synthesized by modulating the gas atmosphere during photoreduction. Hereafter, unless further stated, the following discussion would focus mainly on the characterization of Pt (0.5 wt%) doped BOB in an oxygen atmosphere ( $\text{Pt}_1/\text{BOB-V}_\text{O}$ ), which exhibited the best  $\text{N}_2$  photoreduction of ammonia activity. SEM images of BOB (Fig. S4) and  $\text{Pt}_1/\text{BOB-V}_\text{O}$  (Fig. 1b) indicated that both were composed of nanosheets and that Pt doping has no significant effect on particle size. As disclosed in Fig. S5, the lattice fringes of  $\text{Pt}_1/\text{BOB-V}_\text{O}$  were determined to be 0.282 nm, indicating the formation of BOB with {Abdi, #3787} dominant facets. Furthermore, aberration-corrected high angle annular dark field scanning transmission electron microscopy (AC-HAADF-STEM) was used to visualize Pt species in  $\text{Pt}_1/\text{BOB-V}_\text{O}$  catalyst at the atomic scale. As shown in Figs. 1c-1d, any visible Pt clusters or nanoparticles were not observed in  $\text{Pt}_1/\text{BOB-V}_\text{O}$ , implying that Pt species were atomically dispersed on the BOB surface. However, because of closely atomic number of Pt ( $z = 78$ ) and Bi ( $z = 83$ ), the Pt species were hardly identified as isolated bright dots by the HAADF-STEM images. In addition, Scanning TEM (STEM) and corresponding Energy-dispersive X-ray spectroscopy (EDX) mapping revealed that Bi, O, Br and Pt elements were uniformly dispersed in  $\text{Pt}_1/\text{BOB-V}_\text{O}$  (Figs. 1e-1i). Meanwhile, Pt content in  $\text{Pt}_1/\text{BOB-V}_\text{O}$  measured by ICP-OES was 0.481 wt%, basically in accordance with the Pt/Bi feed ratio, which confirmed the structure of the single-atom  $\text{Pt}_1/\text{BOB-V}_\text{O}$ . To further demonstrate the applicability of the photoreduction strategy, BOB nanosheets doped

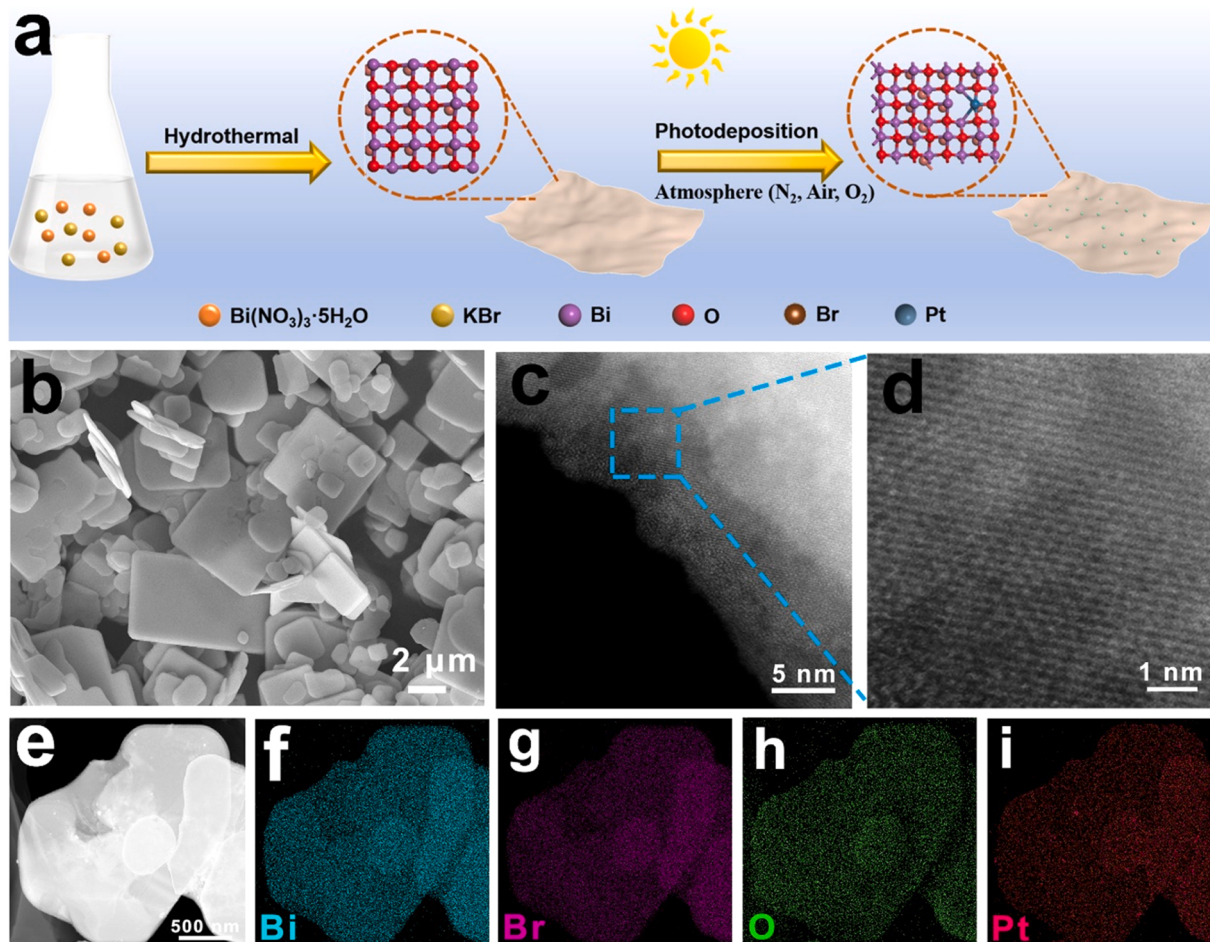


**Fig. 1.** (a) Schematic illustration of the design and preparation of  $\text{Pt}_1/\text{BOB-V}_\text{O}$ , (b) SEM image, (c, d) AC HAADF-STEM images of  $\text{Pt}_1/\text{BOB-V}_\text{O}$  at different magnifications, (e) STEM image and (f-i) corresponding EDX elemental mapping profiles of  $\text{Pt}_1/\text{BOB-V}_\text{O}$  with Bi (blue), Br (pink), O (green), and Pt (red) distribution.

with different metals, such as Pd, Au, Ru and Ag (Figs. S6–S9) have been synthesized. Ultimately, the obtained catalysts were examined for photocatalytic NRR to select the best additives and to analyze in depth the mechanism of activity enhancement.

Fig. 2a showed the XRD patterns of pristine BOB, BOB-V<sub>O</sub> and Pt<sub>1</sub>/BOB-V<sub>O</sub>. It was apparent that all three samples matched well with that of tetragonal phase BiOBr (JCPDS No. 03–0733). No characteristic peaks of Pt compounds were observed, indicating that neither Pt doping nor the introduction of OVs affected the crystalline phase of BOB. More specifically, the diffraction peaks of Pt<sub>1</sub>/BOB-V<sub>O</sub> were gradually shifting towards larger diffraction angles with Pt doping in the magnified figure (Fig. S10), indicating that Pt has been successfully doped into the BOB and caused lattice distortion [36]. The XPS spectra of Pt<sub>1</sub>/BOB-V<sub>O</sub> confirmed the presence of the elements Pt, Bi, Br and O (Fig. S11). As shown in Fig. 2b, for pure BOB, two characteristic peaks centered at binding energies of 159.2 eV and 164.4 eV appeared in the Bi4f spectrum, corresponding to Bi4f<sub>7/2</sub> and 4f<sub>5/2</sub>, respectively [37]. Three peaks were obtained by the deconvolution of O1s spectrum (Fig. 2c) with the largest peak occurring at 529.9 eV, which could be assigned to lattice oxygen (O<sub>L</sub>). Two additional oxygen peaks at 531.6 eV and 533.1 eV, attributed to oxygen vacancies (O<sub>V</sub>) and surface chemisorbed oxygen (O<sub>C</sub>), respectively [38–40]. It was apparent that OVs were formed during the UV treatment. Moreover, the formation of OVs of BOB has been promoted with Pt doping. Considering an extremely low Pt atom content, the OVs should mainly originate from BOB. Furthermore, vacancies were detected by EPR measurement (Fig. 2d). A signal of OVs at a g value of 2.002 was observed for all catalysts [41]. The OVs concentration of Pt<sub>1</sub>/BOB-V<sub>O</sub> was the highest, while the weakest EPR signal was observed for the BOB, which was consistent with XPS results. Surface oxygen vacancies regarded as photocatalytic sites for NRR [42,43]. To clarify this assumption, DFT calculations were further performed (Fig. 2e) and showed that Pt<sub>1</sub>/BOB-V<sub>O</sub> had lower formation energy of OVs (2.68 eV) than BOB (3.20 eV). It was evident that the introduction of Pt on BOB facilitated the formation of surface OVs due to charge

compensation between Pt and lattice defects. Therefore, the modulated local electronic structure of EMSI effect between BOB in conjunction with Pt was carefully observed. As can be seen in Fig. 2b and c, there was a significant red shift for the binding energy in both the Bi4f and O1s of Pt<sub>1</sub>/BOB-V<sub>O</sub>, resulting from Pt doping into the lattice of the BOB. A strong EMSI effect existed between Pt and BOB, where electrons can be efficiently transferred from BOB to Pt due to the attracting electron effect of Pt. As illustrated in the Pt 4f core level spectra (Fig. 2f), it can be noted that the Pt 4f spectra of the samples all showed four peaks after Pt doping. For Pt<sub>1</sub>/BOB-V<sub>O</sub>, binding energies close to 73.1 eV and 76.4 eV were attributed to Pt<sup>2+</sup>, while Pt<sup>4+</sup> appeared at much higher values of about 74.9 eV and 78.2 eV [44,45]. The Pt element appeared in the +4 valence and +2 valence oxidation states rather than the metallic state, supporting the presence of Pt-O bonds between the Pt atom and the oxygen atom. Interestingly, in the spectrum of Pt<sub>1</sub>/BOB-V<sub>O</sub> spectrum, the XPS analysis of Pt<sup>4+</sup>/Pt<sup>2+</sup> ratio was significantly higher than that of Pt/BOB-V<sub>O</sub> (N<sub>2</sub>) and Pt/BOB-V<sub>O</sub> [46]. The above results suggested that photodeposition under different atmospheres can significantly alter the distribution of Pt 4f nuclear electrons, which may lead to strong metal-carrier interactions between Pt and BOB. Further, the formation of photo-deposited Pt in BOB under oxygen atmosphere was analyzed in depth. BOB dispersed in aqueous solution exhibited a positive zeta potential of 8.5 mV (Fig. S12). Then, H<sub>2</sub>PtCl<sub>6</sub>•6H<sub>2</sub>O produced negatively charged PtCl<sub>6</sub><sup>2-</sup> ions while dissolved in deionized water [47]. Upon addition of the PtCl<sub>6</sub><sup>2-</sup> precursor to the BOB mixture, the positively charged BOB was able to strongly adsorb PtCl<sub>6</sub><sup>2-</sup>. Additionally, the electronic structures of Pt<sub>1</sub>/BOB-V<sub>O</sub>, Pt/BOB-V<sub>O</sub> (N<sub>2</sub>) and Pt/BOB-V<sub>O</sub> were investigated by XPS. In contrast, the O 1s (Fig. S13) and Bi 4f spectra (Fig. S14) of Pt<sub>1</sub>/BOB-V<sub>O</sub> clearly shifted towards higher binding energies. It implied that there exists a stronger EMSI effects between the Pt single atom and the BOB carrier in Pt<sub>1</sub>/BOB-V<sub>O</sub> providing a more significant metal-to-carrier electron transfer compared to Pt/BOB-V<sub>O</sub> (N<sub>2</sub>) and Pt/BOB-V<sub>O</sub> [23,48,49]. Naturally, the photodeposition of Pt under different atmospheres did not change the crystal structure of BOB

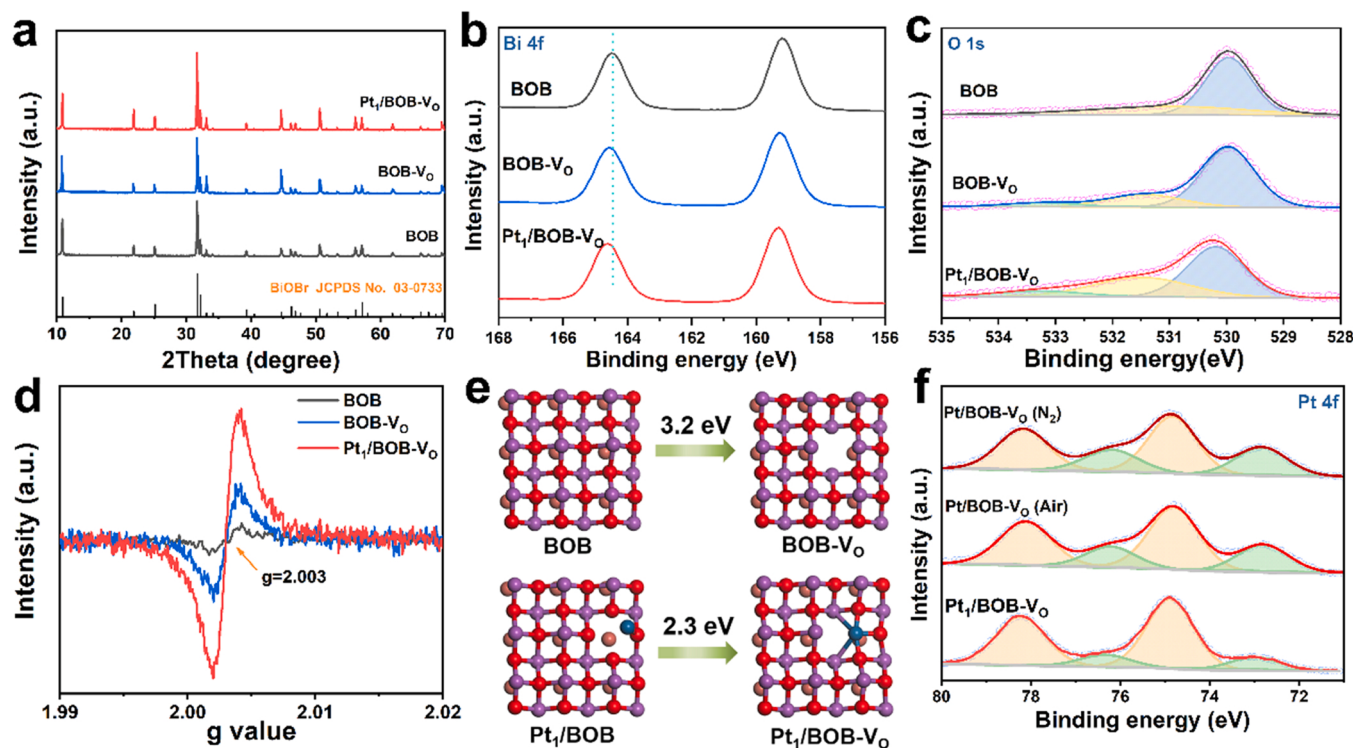


Fig. 2. (a) XRD patterns of BOB, BOB-V<sub>O</sub>, Pt<sub>1</sub>/BOB-V<sub>O</sub>, High-resolution XPS spectra for (b) Bi 4f, (c) O 1s of different samples, (d) EPR spectra of different samples, (e) DFT models for formation energy of oxygen vacancies on BOB-V<sub>O</sub> and Pt<sub>1</sub>/BOB-V<sub>O</sub> and (f) High-resolution XPS spectra for Pt 4f of Pt/BOB-V<sub>O</sub> obtained from different gas atmospheres.

(Fig. S15).

### 3.2. Photocatalytic N<sub>2</sub> fixation tests

N<sub>2</sub> was first introduced into a gas scrubber bottle containing dilute sulphuric acid and water for cleaning to remove any possible N contaminants. Furthermore, N<sub>2</sub> was continuously introduced as feed gas into a quartz reactor for photocatalytic experiments under full-spectrum light irradiation without any sacrificial agent, where N<sub>2</sub> would combine with protons in H<sub>2</sub>O to form ammonia. The concentration of NH<sub>4</sub><sup>+</sup> was quantified by Nessler's reagent and ion chromatography. Encouragingly, the Pt<sub>1</sub>/BOB-V<sub>O</sub> photocatalyst exhibited significant N<sub>2</sub> fixation activity, reflecting the EMSI effect between Pt and BOB. It was demonstrated that the gas atmosphere during Pt photodeposition, metal species and doping amounts affected the photocatalytic ammonia production rates. As shown in Fig. 3a, the highest rate of ammonia synthesis for Pt<sub>1</sub>/BOB-V<sub>O</sub> was achieved with an oxygen atmosphere for photodeposition, probably due to the strong EMSI effect of photodeposited Pt ions with BOB in an oxygen atmosphere. Furthermore, the 0.50 wt% noble metal additive M (M = Pt, Pd, Au, Ru, Ag) was photodeposited onto BOB carriers under an oxygen atmosphere. It was found that the introduction of Pt significantly increased ammonia yield, suggesting a specific role of Pt doping in enhancing the photocatalytic NRR activity (Fig. 3b). Note that strong EMSI between Pt and BOB and Pt doping induced.

enhancement of H\* access and \*N<sub>2</sub> hydrogenation may be key factors, which were examined and discussed in detail below. After successfully obtaining Pt-doped BOB samples, in which the performance of BOB with different Pt contents for photocatalytic N<sub>2</sub> reduction could be investigated. Further optimization of the Pt contents revealed that all X %·BOB samples exhibited N<sub>2</sub> fixation activity. The ammonia evolution rates were in the order of 0.5%-BOB (23.8 μmol g<sup>-1</sup> h<sup>-1</sup>) > 1.0%- BOB (19.5 μmol g<sup>-1</sup> h<sup>-1</sup>) > 0.75%- BOB (19.3 μmol g<sup>-1</sup> h<sup>-1</sup>) > 0.25%- BOB (10.2 μmol g<sup>-1</sup> h<sup>-1</sup>) > 0.1%- BOB (6.0 μmol g<sup>-1</sup> h<sup>-1</sup>) > 0.0%- BOB (2.14 μmol g<sup>-1</sup> h<sup>-1</sup>), higher than Bulk-BOB (Fig. 3c). The decrease in activity

with a further increase in Pt concentration to 1.0 wt% could be attributed to saturation of the active sites at higher doping amounts. Considering EMSI effect on photocatalytic NRR performance, we performed comparative experiments on Pt<sub>1</sub>/BOB-V<sub>O</sub>, BOB-V<sub>O</sub> and BOB-V<sub>O</sub> (Fig. 3d). It was revealed that BOB had almost no nitrogen fixation activity, and the ammonia yield on BOB-V<sub>O</sub> was slightly increased by the introduction of OVs under the same reaction conditions, while the ammonia yield on Pt<sub>1</sub>/BOB-V<sub>O</sub> was significantly increased. With the increase of reaction time, the concentration of ammonia on Pt<sub>1</sub>/BOB-V<sub>O</sub> increased linearly, and the ammonia yield reached 132.5 μmol g<sup>-1</sup> after 6 h. For comparison, the oxygen vacancies were filled by air calcination of Pt<sub>1</sub>/BOB-V<sub>O</sub>. The EPR (Fig. S16) results showed that the oxygen vacancy content of Pt/BOB was very weak after calcination. The ammonia synthesis activity was about 3.2 μmol g<sup>-1</sup> h<sup>-1</sup>, indicating a obvious EMSI effect between BOB and the Pt to improve the photocatalytic N<sub>2</sub> fixation activity of Pt<sub>1</sub>/BOB-V<sub>O</sub>. Ammonia was not detected in six consecutive hours of testing under no photocatalyst, no light or Ar atmosphere. Meanwhile, the isotopic labelling measurements based on <sup>1</sup>H nuclear magnetic resonance (NMR) were carried out to investigate the origination of the N source (Fig. S17). Clearly, when <sup>14</sup>N<sub>2</sub> was used as the feeding gas, a triplet state coupling corresponding to <sup>14</sup>NH<sub>4</sub><sup>+</sup> could be found in the <sup>1</sup>H NMR spectrum. No <sup>14</sup>NH<sub>4</sub><sup>+</sup> signal was observed when Ar bubbled or placed in the dark for 24 h, suggesting that ammonia production was not impurities from the catalyst or solution. This indicated that the process was synergistic between light, catalyst and N<sub>2</sub> as well as provided conclusive evidence for the absence of any N-containing contaminants in the photocatalyst. In addition, there was no significant decrease in ammonia synthesis efficiency during five consecutive measurements, providing excellent recyclability, favorable activity and stability of Pt<sub>1</sub>/BOB-V<sub>O</sub> catalyst (Fig. 3e). No aggregation of Pt atoms (Fig. S18), changes in crystal structure (Fig. S19) or absorbance (Fig. S20) were also observed after the reaction, indicating excellent durability of the photocatalyst. A series of controlled experiments were carried out to exclude any possible NO<sub>x</sub> and NH<sub>3</sub> contaminants.

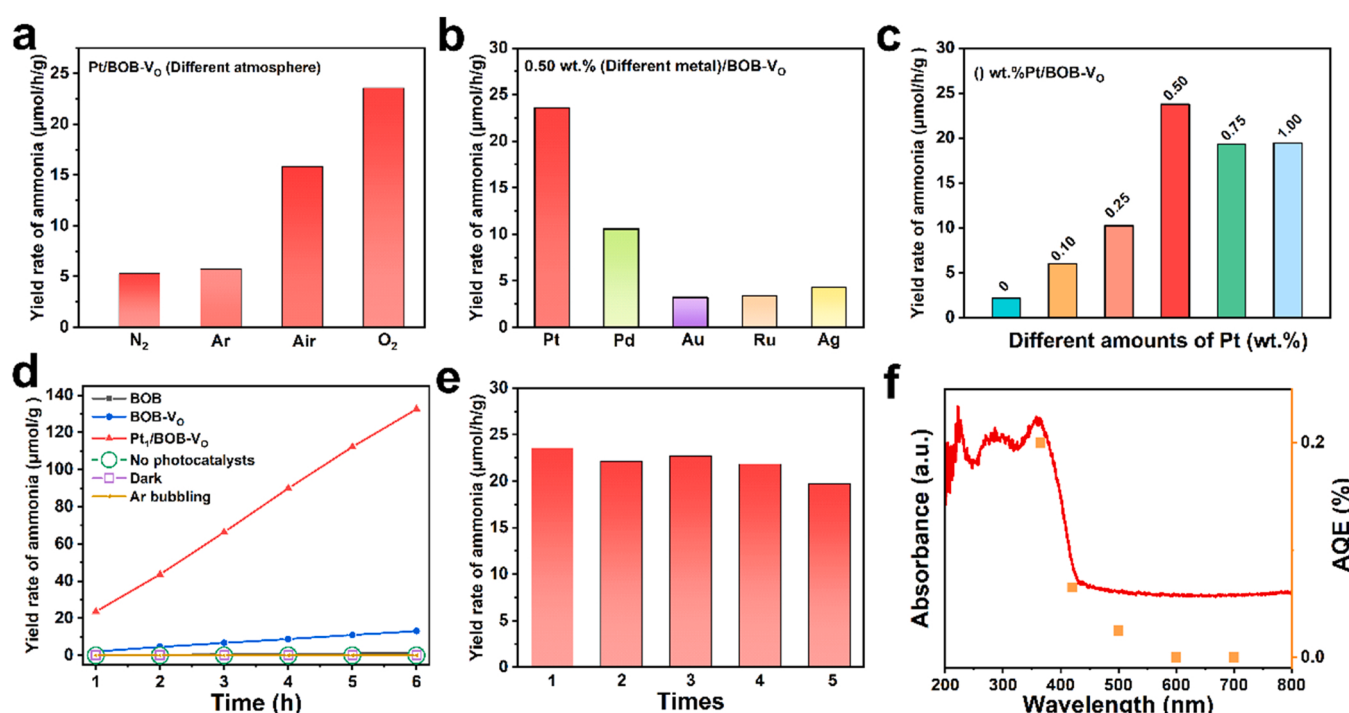


Fig. 3. Photocatalytic N<sub>2</sub> fixation performances of (a) Pt/BOB obtained from different deposition gas atmospheres, (b) M/BOB-V<sub>O</sub> (M = Pt, Pd, Au, Ru, Ag) and (c) BOB with different Pt doping amounts, (d) Time-dependent production of photocatalytic ammonia production of samples under different conditions, (e) Photocatalytic ammonia production rates for cyclic tests of Pt<sub>1</sub>/BOB-V<sub>O</sub> and (f) Calculated AQEs (orange dots) for N<sub>2</sub> fixation over Pt<sub>1</sub>/BOB-V<sub>O</sub> along with its light absorption spectrum (red line).

Specifically, no  $\text{N}_2\text{H}_4$  was detected in the photocatalytic process and only minor traces of nitrate ( $3.5 \mu\text{mol g}^{-1} \text{h}^{-1}$ ), implying an excellent selectivity of  $\text{Pt}_1/\text{BOB-V}_\text{O}$  for the evolution of ammonia. To evaluate the utilization efficiency of light, the wavelength-dependent AQE was assessed by different monochromatic light exposures. As shown in Fig. 3f, the AQE decreased with increasing monochromatic light wavelength, which matched well with the absorption edge of  $\text{Pt}_1/\text{BOB-V}_\text{O}$ . The AQEs at  $\lambda = 365$  and  $420 \text{ nm}$  were calculated as 0.20% and 0.07%, respectively, suggesting a better utilization of incident light, well matched with the light absorption capacity of  $\text{Pt}_1/\text{BOB-V}_\text{O}$ .

### 3.3. Exploration of active sites

The active site of  $\text{N}_2$  adsorption was evaluated by  $\text{N}_2$  TPD method. As shown in Fig. 4a, the desorption signal peak for  $\text{N}_2$  of pristine BOB was weak. The desorption peak of BOB appeared at  $290^\circ\text{C}$ , indicating that OVs promoted  $\text{N}_2$  adsorption at a certain level. While a new desorption peak at  $410^\circ\text{C}$  was observed for  $\text{Pt}_1/\text{BOB-V}_\text{O}$ , indicating that Pt doping provided a new active site for the adsorption of  $\text{N}_2$ . In addition, the position of the peak located at  $290^\circ\text{C}$  shifted towards higher temperatures compared to  $\text{BOB-V}_\text{O}$ , indicating that the increase of oxygen vacancies in  $\text{Pt}_1/\text{BOB-V}_\text{O}$  promoted  $\text{N}_2$  chemisorption capacity. Consequently, the synergistic effect of the exposed metal dopant and OVs can also promote  $\text{N}_2$  adsorption and activation. Thus, the defective energy levels introduced by Pt doping would act as electron capture sites, thus further enhancing the activation and reaction of the  $\text{N}_2$  molecule via accelerating the transfer of photogenerated electrons from

the  $\text{BOB-V}_\text{O}$ -Strain (i.e. conduction band electrons) to the  $\pi^*$  antibonding orbitals of the  $\text{N}_2$  [50].

The transfer paths of photoexcited charges on synthetic  $\text{Pt}_1/\text{BOB-V}_\text{O}$  were recorded using in-situ XPS. As can be seen in Fig. 4b, two additional peaks at lower binding energies of Bi 4 f peak were observed on  $\text{Pt}_1/\text{BOB-V}_\text{O}$  under irradiation, corresponding to OV-connected Bi in the lower valence state. Furthermore, EMSI effect resulted in the formation of oxygen vacancies due to the difference in valence between Pt and Bi, which enabled effective adsorption and activation of  $\text{N}_2$  and reduces photogenerated carrier recombination. In order to better understand the changes in Pt valence during  $\text{N}_2$  fixation, in situ XPS measurements of  $\text{Pt}_1/\text{BOB-V}_\text{O}$  were carried out. As shown in the Pt 4 f XPS spectrum (Fig. 4c), there was a partial shift in the Pt valence state from +4 to +2 valence after treating the sample with  $\text{N}_2$  gas and irradiating it, and the binding energy of the Pt 4 f peak decreased slightly, indicating that the Pt site on  $\text{Pt}_1/\text{BOB-V}_\text{O}$  can obtain photogenerated electrons in the  $\text{N}_2$  reduction reaction [51]. After photocatalytic nitrogen fixation reaction,  $\text{Pt}_1/\text{BOB-V}_\text{O}$  turned from earthy yellow to grey in color (Fig. S21a), indicating the presence of the lower valence Pt. More importantly, after switching off the light and introducing oxygen for 30 min, the Pt sites gradually returned to their initial oxidation state while the  $\text{Pt}_1/\text{BOB-V}_\text{O}$  turned earthy yellow (Fig. S21b), thus demonstrating good photostability of  $\text{Pt}_1/\text{BOB-V}_\text{O}$ . Based on the above discussion, the strategy for the synthesis of  $\text{Pt}_1/\text{BOB-V}_\text{O}$  catalysts, and the mechanism of charge transfer and valence change under illumination can be summarized as Fig. 4d. Firstly, a strong EMSI between the photodeposited Pt atom and BOB in an oxygen atmosphere led to a positively charged state of the Pt

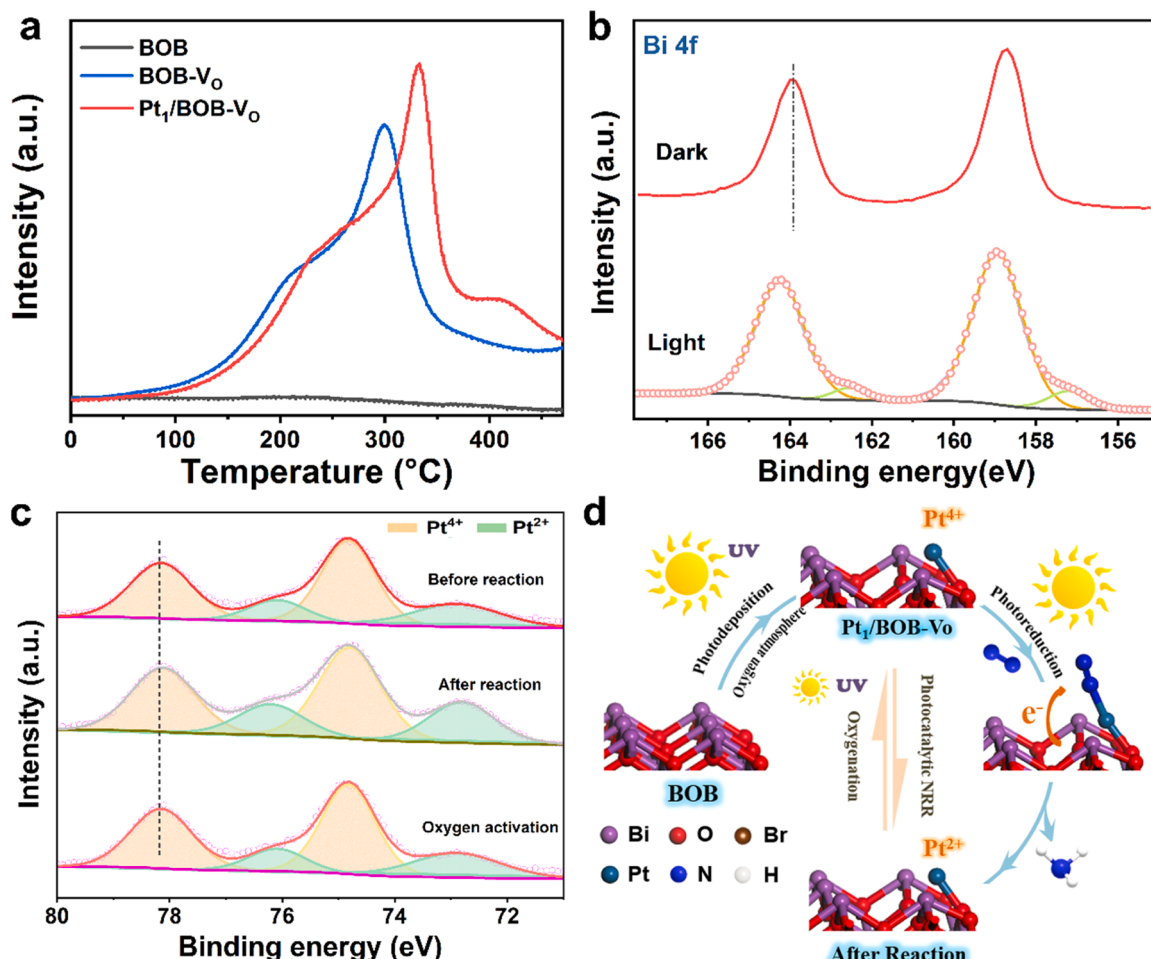


**Fig. 4.** (a)  $\text{N}_2$  TPD of BOB,  $\text{BOB-V}_\text{O}$  and  $\text{Pt}_1/\text{BOB-V}_\text{O}$ , (b) In-situ XPS spectra for Bi 4 f treating with  $\text{N}_2$  and irradiation, (c) XPS spectra of Pt 4 f treating with different conditions of  $\text{Pt}_1/\text{BOB-V}_\text{O}$  and (d) Illustration of charge transfer and valence variation on  $\text{Pt}_1/\text{BOB-V}_\text{O}$  for photocatalytic NRR.

configuration (mainly  $\text{Pt}^{4+}$ ) and promoted the production of oxygen vacancies. Interestingly, the oxygen vacancy and  $\text{Pt}^{4+}$  sites may be synergistic active sites for photocatalytic  $\text{N}_2$  reduction. Under illumination, the atomically active site  $\text{Pt}^{4+}$  can gain photogenerated electrons to reduce the valence state ( $\text{Pt}^{2+}$ ) in NRR. Moreover, after UV-lamp treatment in an oxygen atmosphere,  $\text{Pt}^{2+}$  can be returned via direct electron transfer back through  $\text{Pt}^{4+}$ , resulting in a redox cycle of  $\text{Pt}^{4+} \rightarrow \text{Pt}^{2+} \rightarrow \text{Pt}^{4+}$  and regeneration of the Pt active site.

### 3.4. Optical and electronic properties

By analyzing the essential influences on the photocatalytic  $\text{N}_2$  fixation process including light absorption, charge transfer kinetics and surface catalytic reactions, the performance enhancement mechanism of  $\text{Pt}_1/\text{BOB-V}_\text{O}$  relative to  $\text{BOB-V}_\text{O}$  and BOB samples was adequately elucidated. In order to clarify the basis for the enhanced photocatalytic activity, we first investigated the light absorption properties of the samples. It can be observed from UV-vis DRS, the pure BOB showed a steep absorption edge at about 430 nm, which can be defined as the intrinsic band gap absorption of BOB (Fig. 5a). When oxygen vacancies were introduced by photoreduction, the  $\text{BOB-V}_\text{O}$  absorption edge was slightly red-shifted and the light absorption intensity increased. This is due to the formation of impure energy levels in the band gap of the BOB, which narrowed the band gap [42,52]. In addition, after depositing Pt on the BOB surface, the light absorption range of  $\text{Pt}_1/\text{BOB-V}_\text{O}$  gradually expanded and the light intensity gradually increased. The variation of the color of samples also reflected the light absorption characteristics (Fig. S22), which increased significantly with the deepening of the sample color. It has been speculated that the increase in oxygen vacancies due to Pt doping and the incorporation of PtO species on the

catalyst surface could enhance the light absorption intensity of  $\text{Pt}_1/\text{BOB-V}_\text{O}$ . As a result, a narrowing of the band gap of the  $\text{Pt}_1/\text{BOB-V}_\text{O}$  material can be observed. The UV-vis DRS absorption spectra were converted to the corresponding Tauc plots (Fig. S23), with band gap energies of 2.80 eV, 2.72 eV and 2.50 eV for BOB,  $\text{BOB-V}_\text{O}$  and  $\text{Pt}_1/\text{BOB-V}_\text{O}$ , respectively, based on the tangent intercepts of the plots. Crucially, the band gap and density of states (DOS) of BOB,  $\text{BOB-V}_\text{O}$  and  $\text{Pt}_1/\text{BOB-V}_\text{O}$  were investigated by DFT calculations (Fig. S24). The pure BOB showed a band gap of 2.15 eV between a VBM (dominated by Br 4p states) and a CBM (dominated by Bi 6p states). For  $\text{BOB-V}_\text{O}$ , a narrower band gap and a new defect state were observed. In the presence of the OV and Pt introduction, impurity energy levels appeared at both VB and CB. A similar structure could be observed in (Pd, Au, Ru, Ag)/BOB-V<sub>O</sub> (Figs. S25–S28), indicating that metal doping changed the electron density and composition of VB and VBM, significantly shortening the band gap of BOB. A level of defects introduced by Pt doping can be assumed to act as electron capture points to accelerate the transfer of photo-generated electrons from BOB to Pt, as can be further demonstrated by experimental photoelectrochemical measurements. Furthermore, XPS valence band spectroscopy (Fig. S29a) suggested that the VB energy levels of BOB,  $\text{BOB-V}_\text{O}$  and  $\text{Pt}_1/\text{BOB-V}_\text{O}$  were 2.06 eV, 1.91 eV and 1.59 eV, respectively. Therefore, the corresponding conduction bands were calculated as –0.74 eV, –0.81 eV and –0.91 eV for BOB,  $\text{BOB-V}_\text{O}$  and  $\text{Pt}_1/\text{BOB-V}_\text{O}$  respectively, according to band gap equation ( $E_\text{g} = E_\text{VB} - E_\text{CB}$ ), as shown in Fig. S29b. Therefore, the light absorption and energy band results indicated that  $\text{Pt}_1/\text{BOB-V}_\text{O}$  promoted incident light absorption to facilitate the generation of more photo-generated carriers, resulting in efficient NRR activity.

Photoluminescence spectroscopy was a valuable measure to examine the separation efficiency of photoexcited electron-hole pairs, in general,

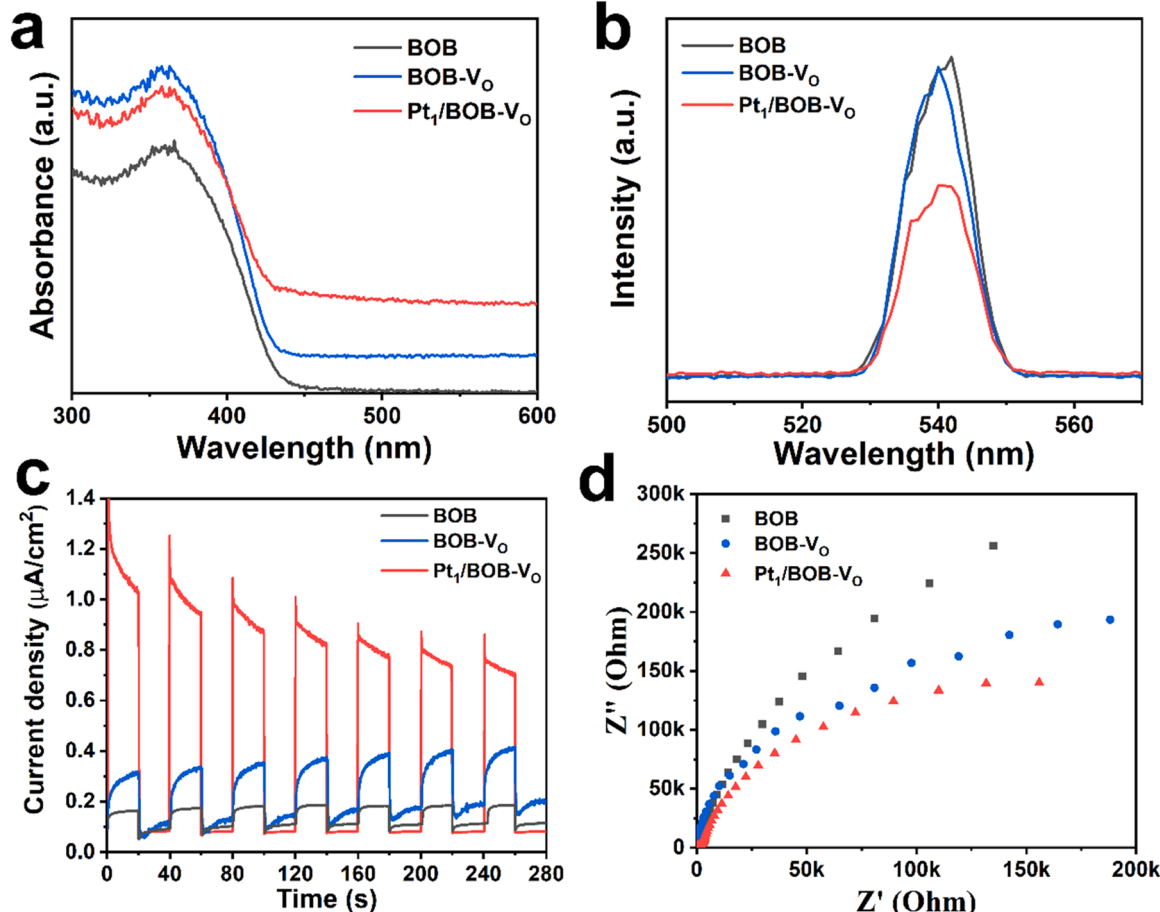


Fig. 5. (a) DRS spectra, (b) PL spectra, (c) Photocurrent responses, (d) EIS of BOB,  $\text{BOB-V}_\text{O}$  and  $\text{Pt}_1/\text{BOB-V}_\text{O}$ .

weak PL intensities indicating a low rate of photo-generated electron-hole complexation under illumination [53]. As shown in Fig. 5b, BOB-Vo exhibited a slightly lower quenched PL intensity than BOB, showing that more unpaired electrons and oxygen defect energy levels are generated upon the introduction of oxygen vacancies. Time-resolved photoluminescence (TR-PL) was applied to study the charge separation on BOB and BOB-V<sub>O</sub> samples (Fig. S30). The average fluorescence lifetime for BOB and BOB-V<sub>O</sub> was measured as 1.335 ns and 1.474 ns, respectively. This minor variation might be attributed to the oxygen vacancy being more prone to form trap states, trapping excited state electrons and inhibiting the direct compounding of photogenerated carriers, which could extend the lifetime of photogenerated electrons. In addition, the PL intensity of Pt<sub>1</sub>/BOB-Vo distinctly decreased compared to that of BOB-Vo, indicating that the EMSI effect facilitated interfacial charges transfer. As expected, the Pt<sub>1</sub>/BOB-Vo response exhibited a higher current density than that of BOB-Vo and pure BOB (Fig. 5c). This phenomenon suggested that photogenerated electron-holes complexation was greatly suppressed, consistent with the PL analysis. Furthermore, it was also supported by the EIS spectra (Fig. 5d), where BOB showed the largest Nyquist plot semicircle, indicating the highest charge transfer resistance [54]. The diameter of the high-frequency semicircle of Pt<sub>1</sub>/BOB-Vo was much smaller than that of BOB-Vo and BOB, further indicating a much lower interfacial charge transfer resistance between Pt and BOB-Vo, thus achieving rapid separation and migration of photogenerated carriers. The above results showed that the presence of EMSI between Pt and BOB reduced the contact resistance and energy barriers at the metal/carrier interface, enabling the formation of efficient channels that facilitate the transfer of charge and efficient separation of carriers.

### 3.5. The reaction mechanism of photocatalytic nitrogen fixation

DFT calculations have been employed for an in-depth analysis of the active site and the corresponding electronic structure to further propose the mechanism of EMSI effect on NRR. Initially, the charge density difference further revealed the discrete nature of the charge distribution in Pt<sub>1</sub>/BOB-Vo, with the yellow and blue regions representing the increase and decrease in charge density, respectively. As can be seen in Fig. 6a, there was a significant charge accumulation around Pt and a significant charge depletion around Bi, indicating that a strong EMSI between Pt atoms and BOB. The charge density difference of Pt<sub>1</sub>/BOB-Vo with N<sub>2</sub> adsorption was further calculated as in Fig. 6b. Electrons tended to transfer from the catalyst to N<sub>2</sub> and the bond length of N<sub>2</sub> was significantly extended from 1.112 to 1.131 Å (Fig. S31) [55,56]. Meanwhile, Bader charge analysis revealed that the transfer of 0.25 e- to N<sub>2</sub>. A strong EMSI between Pt synergistic oxygen vacancies and N<sub>2</sub> was further demonstrated, resulting in promoting N<sub>2</sub> activation and improving NRR performance. To reveal the modulation effect of EMSI on the hydrogenation reaction pathway of N<sub>2</sub> molecules in NRR over Pt<sub>1</sub>-BOB-V<sub>O</sub> at the atomic scale, DFT calculation was further employed to further simulate the Gibbs free energy of NRR complete pathway. Clearly, NRR preferred to be hydrogenated via alternating pathways, with N<sub>2</sub> fixation route of the reaction energy process of \*N<sub>2</sub> → \*NNH → \*NNH<sub>2</sub> → \*NH<sub>2</sub>NH<sub>2</sub> → \*NH<sub>2</sub>NH<sub>2</sub> → \*NH<sub>2</sub> + \*NH<sub>3</sub> → \*NH<sub>2</sub> → \*NH<sub>3</sub> → NH<sub>3</sub>. For the original BOB, N<sub>2</sub> adsorption free energy was 0.69 eV, implying that it was very difficult for BOB to adsorb N<sub>2</sub> on its surface (Fig. 6c), which was in consistent with N<sub>2</sub>-TPD results. Furthermore, it determined the rate limiting step of N<sub>2</sub>\* to NNH\* at an energy barrier of 1.90 eV on BOB due to the inertness and stability of N<sub>2</sub>. When introduced into oxygen vacancies on BOB surface, it can improve N<sub>2</sub> adsorption in the initial reaction step of the NRR reaction (Fig. 6d). The free energy of N<sub>2</sub> adsorption was 0.56 eV, which was significantly lower than that of the original BOB. It indicated that the N<sub>2</sub> molecule tended to adsorb to the oxygen vacancy, but the Gibbs free energies of the first step of the hydrogenation reaction on BOB-V<sub>O</sub> (\*N<sub>2</sub> + (H<sup>+</sup> + e<sup>-</sup>) → \*NNH) was 1.86 eV, exhibiting the largest energy barrier. Most

importantly, the adsorption of N<sub>2</sub> molecules followed by hydrogenation to produce N<sub>2</sub>H\* was often considered the central intermediate in NRR, and this process was the rate-controlling step in the overall N<sub>2</sub> fixation process. Therefore, a highly active NRR catalyst should facilitate the generation of \*N<sub>2</sub>H [8,16]. As can be seen from Fig. 6e, the chemical bonding of the adsorbed N<sub>2</sub> (\*N<sub>2</sub>) was significantly weakened due to EMSI effect of Pt<sub>1</sub>/BOB-V<sub>O</sub>. Strong EMSI in Pt<sub>1</sub>/BOB-V<sub>O</sub> also induced electron redistribution around Pt, which may favor the adsorption of reaction intermediates on Pt sites.

Consequently, the reaction potential of the hydrogenation reaction of \*N<sub>2</sub> on Pt<sub>1</sub>/BOB-V<sub>O</sub> was 0.71 eV, which was much lower than that of BOB-V<sub>O</sub> and BOB, demonstrating that Pt doping can enhance its initial hydrogenation reaction from a thermodynamic point. Further, subsequent hydrogenation of N-NH\* to N-NH<sub>2</sub>\* on Pt<sub>1</sub>/BOB-V<sub>O</sub> surface required a reaction energy of 0.69 eV. The calculations demonstrated that the subsequent hydrogenation process of \*NNH<sub>2</sub> followed an energy-decreasing path of spontaneous hydrogenation and the energy, ZPE and entropy contribution were provided in Table S1. Furthermore, the H<sub>2</sub>O\*, H\* and OH\* adsorption energies of BOB, BOB-V<sub>O</sub> and Pt<sub>1</sub>/BOB-V<sub>O</sub> were calculated to explore the key role of Pt doping, with the relevant adsorption model shown in Fig. S32. Compared to BOB and BOB-V<sub>O</sub>, the ammonia production rate of Pt<sub>1</sub>/BOB-V<sub>O</sub> can be substantially enhanced by using water as a proton source. The enhanced activity could be attributed to the facilitated adsorption with H<sub>2</sub>O\* and OH\* - through Pt doping (Fig. S33). Meanwhile, the potential barrier dropped to -0.54 eV when Pt atoms were doped into BOB-V<sub>O</sub>, indicating a more efficient access to H\* on the surface of Pt<sub>1</sub>/BOB-V<sub>O</sub>. In summary, the generation of oxygen vacancies can be promoted by Pt doping, thus facilitating the chemisorption of N<sub>2</sub> on the catalyst surface. The electron-rich Vo site enhanced electrons transfer to N<sub>2</sub> molecules, thus achieving N<sub>2</sub> activation. Therefore, the dramatically enhanced activity of Pt<sub>1</sub>/BOB-V<sub>O</sub> was due to the availability of sufficient H\* supply, which greatly facilitated the hydrogenation of N<sub>2</sub> and the formation of ammonia. In summary, the EMSI effect had two main positive effects in photocatalytic NRR: Strong EMSI effect between Pt and BOB effectively accelerated photoelectron transfer from BOB to Pt sites for NRR; and (2) The EMSI effect led to a significant charge redistribution between Pt and BOB carriers, which reduced the energy barrier associated with N<sub>2</sub> activation and hydrogenation.

## 4. Conclusions

In summary, we have firstly designed and synthesized functional Pt<sub>1</sub>/BOB-V<sub>O</sub> toward photocatalytic N<sub>2</sub> reduction. In situ XPS spectra revealed that the Pt site received photoexcited electrons to promote N<sub>2</sub> activation during NRR, suggesting that EMSI effects can modulate the active site during the reaction. Theoretical calculations and experimental results showed that atomically dispersed Pt stably doped on BOB carriers was designed to with strong EMSI, which led to an electron-rich environment for NRR. Such a strong EMSI effect induces electrons localization to the active Pt center, lowering the energy barrier of the nitrogen reduction rate limiting step (\*N<sub>2</sub> + (H<sup>+</sup> + e<sup>-</sup>) → \*NNH) and allowing the hydrogenation reaction of N<sub>2</sub> to follow a conjoined alternating pathway. Moreover, it was demonstrated the optimized Pt<sub>1</sub>/BOB-V<sub>O</sub> photocatalyst promoted ammonia production at a rate of 23.8 μmol g<sup>-1</sup> h<sup>-1</sup> without any sacrificial agent, which remained favorable stability after four NRR cycles. Researches guide the development of new photocatalysts using EMSI effect and the rational design of catalytic sites to achieve efficient photocatalytic NRR.

## CRediT authorship contribution statement

**Guangmin Ren:** Conceptualization, Methodology, Investigation, Writing – original draft preparation, Writing – review & editing. **Meng Shi:** Conceptualization, Methodology. **Zizhen Li:** Methodology, Writing – original draft preparation, Writing – review & editing. **Zisheng Zhang:**

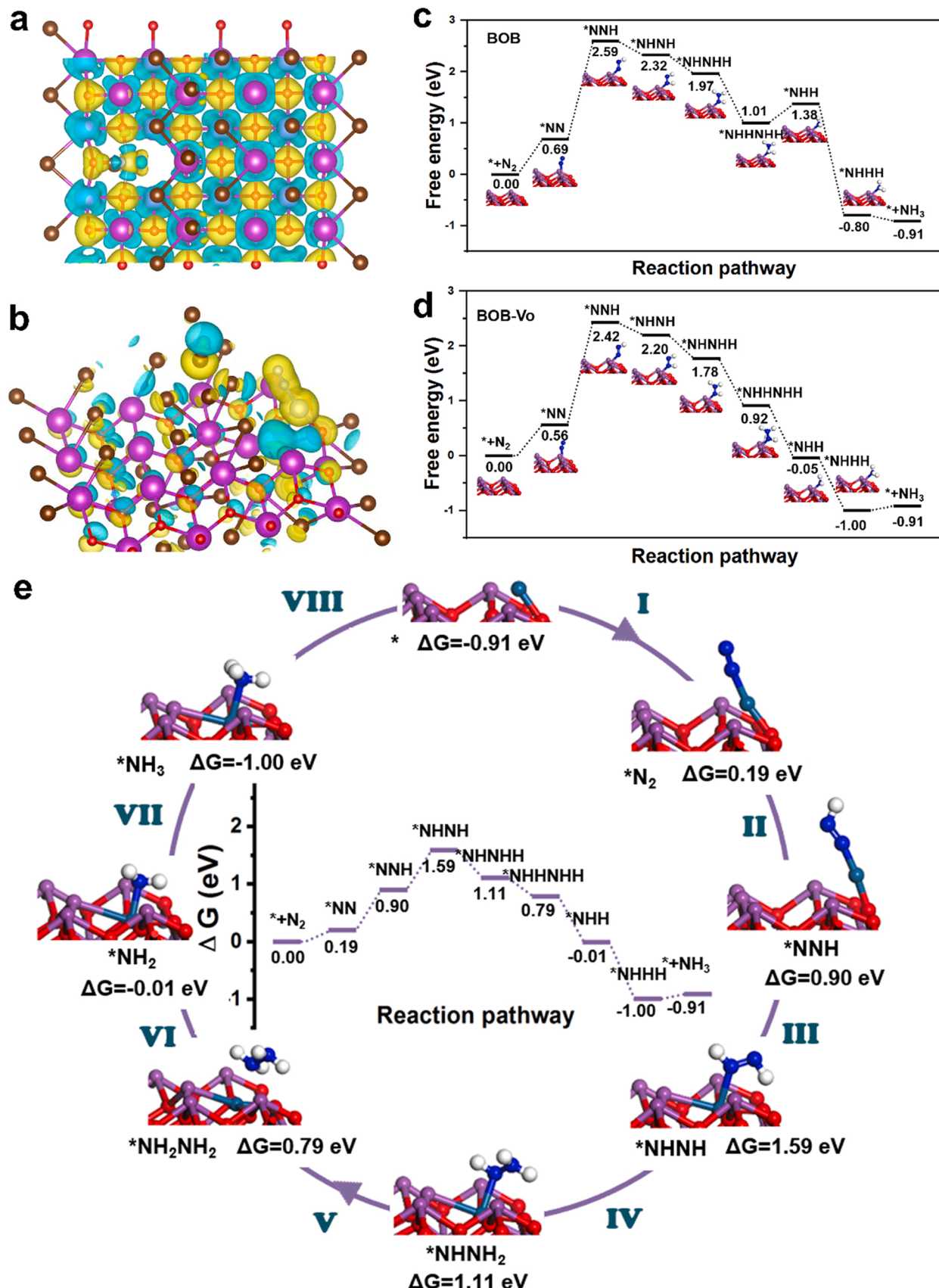


**Fig. 6.** (a) Bader charge density difference of Pt<sub>1</sub>/BOB-V<sub>O</sub>, (b) Differential charge distribution between nitrogen and Pt<sub>1</sub>/BOB-V<sub>O</sub>, Yellow and cyan colors represent electron accumulation and depletion regions, respectively. (c, d, e) Free energy diagram of NRR on BOB, BOB-V<sub>O</sub>, Pt<sub>1</sub>/BOB-V<sub>O</sub> and corresponding optimized geometric structure.

Methodology, Investigation, Writing – review & editing. **Xiangchao Meng**: Supervision, Conceptualization, Writing – original draft, Writing – review & editing.

## Declaration of Competing Interest

The authors declare that they have no known competing financial interests or personal relationships that could have appeared to influence the work reported in this paper.

## Data Availability

Data will be made available on request.

## Acknowledgment

This work was financially supported by the National Natural Science Foundation of China (Grant No: 22002146), Shandong Provincial Natural Science Foundation (Grant No.: ZR2021QB056), China Postdoctoral Science Foundation (Grant No.: 2020M682241), and Taishan Scholars Foundation of Shandong province (No.: tsqn201909058). The authors would like to thank Shiyanjia Lab (<https://www.shiyanjia.com>) for the XRD, SEM, XPS etc. analysis.

## Appendix A. Supporting information

Supplementary data associated with this article can be found in the online version at [doi:10.1016/j.apcatb.2023.122462](https://doi.org/10.1016/j.apcatb.2023.122462).

## References

- [1] X. Cui, C. Tang, Q. Zhang, A review of electrocatalytic reduction of dinitrogen to ammonia under ambient conditions, *Adv. Energy Mater.* 8 (2018) 1800369.
- [2] D.R. MacFarlane, P.V. Cherepanov, J. Choi, B.H.R. Suryanto, R.Y. Hodgetts, J. M. Bakker, F.M. Ferrero Vallana, A.N. Simonov, A roadmap to the ammonia economy, *Joule* 4 (2020) 1186–1205.
- [3] C. Guo, J. Ran, A. Vasileff, S.-Z. Qiao, Rational design of electrocatalysts and photo (electro)catalysts for nitrogen reduction to ammonia (NH<sub>3</sub>) under ambient conditions, *Energy Environ. Sci.* 11 (2018) 45–56.
- [4] G.F. Chen, S. Ren, L. Zhang, H. Cheng, Y. Luo, K. Zhu, L.X. Ding, H. Wang, Advances in electrocatalytic N<sub>2</sub> reduction-strategies to tackle the selectivity challenge, *Small Methods* 3 (2018) 1800337.
- [5] Z. Zhao, S. Hong, C. Yan, C. Choi, Y. Jung, Y. Liu, S. Liu, X. Li, J. Qiu, Z. Sun, Efficient visible-light driven N<sub>2</sub> fixation over two-dimensional Sb/TiO<sub>2</sub> composites, *Chem. Commun.* 55 (2019) 7171–7174.
- [6] C. Ma, Y. Zhang, S. Yan, B. Liu, Carbon-doped boron nitride nanosheets: a high-efficient electrocatalyst for ambient nitrogen reduction, *Appl. Catal. B-Environ.* 315 (2022), 121574.
- [7] R. Guan, D. Wang, Y. Zhang, C. Liu, W. Xu, J. Wang, Z. Zhao, M. Feng, Q. Shang, Z. Sun, Enhanced photocatalytic N<sub>2</sub> fixation via defective and fluoride modified TiO<sub>2</sub> surface, *Appl. Catal. B-Environ.* 282 (2021), 119580.
- [8] J. Li, D. Wang, R. Guan, Y. Zhang, Z. Zhao, H. Zhai, Z. Sun, Vacancy-enabled mesoporous TiO<sub>2</sub> modulated by nickel doping with enhanced photocatalytic nitrogen fixation performance, *ACS Sustain. Chem. Eng.* 8 (2020) 18258–18265.
- [9] B. Sun, Z. Liang, Y. Qian, X. Xu, Y. Han, J. Tian, Sulfur vacancy-rich O-Doped 1T-MoS<sub>2</sub> nanosheets for exceptional photocatalytic nitrogen fixation over CdS, *ACS Appl. Mater. Inter.* 12 (2020) 7257–7269.
- [10] X.H. Li, W.L. Chen, H.Q. Tan, F.R. Li, J.P. Li, Y.G. Li, E.B. Wang, Reduced state of the graphene oxide@polyoxometalate nanocatalyst achieving high-efficiency nitrogen fixation under light driving conditions, *ACS Appl. Mater. Inter.* 11 (2019) 37927–37938.
- [11] H. Li, Y. Liu, Y. Liu, L. Wang, R. Tang, P. Deng, Z. Xu, B. Haynes, C. Sun, J. Huang, Efficient visible light driven ammonia synthesis on sandwich structured C<sub>3</sub>N<sub>4</sub>/MoS<sub>2</sub>/MnO<sub>4</sub> catalyst, *Appl. Catal. B-Environ.* 281 (2021), 119476.
- [12] Y. Xue, Y. Guo, Z. Liang, H. Cui, J. Tian, Porous g-C<sub>3</sub>N<sub>4</sub> with nitrogen defects and cyano groups for excellent photocatalytic nitrogen fixation without co-catalysts, *J. Colloid Interface Sci.* 556 (2019) 206–213.
- [13] G. Zhang, C.D. Sewell, P. Zhang, H. Mi, Z. Lin, Nanostructured photocatalysts for nitrogen fixation, *Nano Energy* 71 (2020), 104645.
- [14] X. Chen, N. Li, Z. Kong, W.-J. Ong, X. Zhao, Photocatalytic fixation of nitrogen to ammonia: state-of-the-art advancements and future prospects, *Mater. Horiz.* 5 (2018) 9–27.
- [15] M. Cheng, C. Xiao, Y. Xie, Photocatalytic nitrogen fixation: the role of defects in photocatalysts, *J. Mater. Chem. A* 7 (2019) 19616–19633.
- [16] X. Bian, Y. Zhao, S. Zhang, D. Li, R. Shi, C. Zhou, L.-Z. Wu, T. Zhang, Enhancing the supply of activated hydrogen to promote photocatalytic nitrogen fixation, *ACS Mater. Lett.* 3 (2021) 1521–1527.
- [17] H. Li, M. Xia, B. Chong, H. Xiao, B. Zhang, B. Lin, B. Yang, G. Yang, Boosting photocatalytic nitrogen fixation via constructing low-oxidation-state active sites in the nanoconfined spinel iron cobalt oxide, *ACS Catal.* 12 (2022) 10361–10372.
- [18] R. Shi, Y. Zhao, G.I.N. Waterhouse, S. Zhang, T. Zhang, Defect engineering in photocatalytic nitrogen fixation, *ACS Catal.* 9 (2019) 9739–9750.
- [19] Z. Zhao, D. Wang, R. Gao, G. Wen, M. Feng, G. Song, J. Zhu, D. Luo, H. Tan, X. Ge, W. Zhang, Y. Zhang, L. Zheng, H. Li, Z. Chen, Magnetic-field-stimulated efficient photocatalytic N<sub>2</sub> fixation over defective BaTiO<sub>3</sub> perovskites, *Angew. Chem. Int. Ed. Engl.* 60 (2021) 11910–11918.
- [20] G. Ren, S. Liu, M. Shi, Z. Zhang, Z. Li, X. Meng, Ultraviolet light-modulated defects on BiOBr to improve the photocatalytic fixation of nitrogen to ammonia, *Sol. RRL* 6 (2022) 2200653.
- [21] M. Li, Q. Lu, M. Liu, P. Yin, C. Wu, H. Li, Y. Zhang, S. Yao, Photoinduced charge separation via the double-electron transfer mechanism in nitrogen vacancies g-C<sub>3</sub>N<sub>4</sub>/BiOBr for the photoelectrochemical nitrogen reduction, *ACS Appl. Mater. Inter.* 12 (2020) 38266–38274.
- [22] H. Li, J. Shang, Z. Ai, L. Zhang, Efficient visible light nitrogen fixation with BiOBr nanosheets of oxygen vacancies on the exposed {001} facets, *J. Am. Chem. Soc.* 137 (2015) 6393–6399.
- [23] T. Wu, X. Zhu, Z. Xing, S. Mou, C. Li, Y. Qiao, Q. Liu, Y. Luo, X. Shi, Y. Zhang, X. Sun, Greatly improving electrochemical N<sub>2</sub> reduction over TiO<sub>2</sub> nanoparticles by iron doping, *Angew. Chem. Int. Ed. Engl.* 58 (2019) 18449–18453.
- [24] B.H. Lee, S. Park, M. Kim, A.K. Sinha, S.C. Lee, E. Jung, W.J. Chang, K.S. Lee, J. H. Kim, S.P. Cho, H. Kim, K.T. Nam, T. Hyeon, Reversible and cooperative photoactivation of single-atom Cu/TiO<sub>2</sub> photocatalysts, *Nat. Mater.* 18 (2019) 620–626.
- [25] Y. Zhao, Y. Zhao, R. Shi, B. Wang, G.I.N. Waterhouse, L.Z. Wu, C.H. Tung, T. Zhang, Tuning oxygen vacancies in ultrathin TiO<sub>2</sub> nanosheets to boost photocatalytic nitrogen fixation up to 700 nm, *Adv. Mater.* 31 (2019), e1806482.
- [26] Y. Zhang, Q. Wang, S. Yang, H. Wang, D. Rao, T. Chen, G. Wang, J. Lu, J. Zhu, S. Wei, X. Zheng, J. Zeng, Tuning the interaction between ruthenium single atoms and the second coordination sphere for efficient nitrogen photofixation, *Adv. Funct. Mater.* 32 (2022) 2112452.
- [27] J. Yang, W.H. Li, S. Tan, K. Xu, Y. Wang, D. Wang, Y. Li, The electronic metal-support interaction directing the design of single atomic site catalysts: achieving high efficiency towards hydrogen evolution, *Angew. Chem. Int. Ed. Engl.* 60 (2021) 19085–19091.
- [28] Y. Shi, Z.R. Ma, Y.Y. Xiao, Y.C. Yin, W.M. Huang, Z.C. Huang, Y.Z. Zheng, F.Y. Mu, R. Huang, G.Y. Shi, Y.Y. Sun, X.H. Xia, W. Chen, Electronic metal-support interaction modulates single-atom platinum catalysis for hydrogen evolution reaction, *Nat. Commun.* 12 (2021) 3021.
- [29] K. Liu, X. Zhao, G. Ren, T. Yang, Y. Ren, A.F. Lee, Y. Su, X. Pan, J. Zhang, Z. Chen, J. Yang, X. Liu, T. Zhou, W. Xi, J. Luo, C. Zeng, H. Matsumoto, W. Liu, Q. Jiang, K. Wilson, A. Wang, B. Qiao, W. Li, T. Zhang, Strong metal-support interaction promoted scalable production of thermally stable single-atom catalysts, *Nat. Commun.* 11 (2020) 1263.
- [30] G. Ren, M. Shi, S. Liu, Z. Li, Z. Zhang, X. Meng, Molecular-level insight into photocatalytic reduction of N<sub>2</sub> over Ruthenium single atom modified TiO<sub>2</sub> by electronic Metal-support interaction, *Chem. Eng. J.* 454 (2023), 140158.
- [31] J. Yang, W.H. Li, K. Xu, S. Tan, D. Wang, Y. Li, Regulating the tip effect on single-atom and cluster catalysts: forming reversible oxygen species with high efficiency in chlorine evolution reaction, *Angew. Chem. Int. Ed. Engl.* 61 (2022), e202200366.
- [32] J. Xu, H. Xu, A. Dong, H. Zhang, Y. Zhou, H. Dong, B. Tang, Y. Liu, L. Zhang, X. Liu, J. Luo, L. Bie, S. Dai, Y. Wang, X. Sun, Y. Li, Strong electronic metal-support interaction between iridium single atoms and a WO<sub>3</sub> support promotes highly efficient and robust CO<sub>2</sub> cycloaddition, *Adv. Mater.* 34 (2022), e2206991.
- [33] M.V. Grabchenko, G.V. Mamontov, V.I. Zaikovskii, V. La Parola, L.F. Liotta, O. V. Vodyankina, The role of metal–support interaction in Ag/CeO<sub>2</sub> catalysts for CO and soot oxidation, *Appl. Catal. B-Environ.* 260 (2020), 118148.
- [34] X. Chen, X. Zhang, Y.-H. Li, M.-Y. Qi, J.-Y. Li, Z.-R. Tang, Z. Zhou, Y.-J. Xu, Transition metal doping BiOBr nanosheets with oxygen vacancy and exposed {102} facets for visible light nitrogen fixation, *Appl. Catal. B-Environ.* 281 (2021), 119516.
- [35] James N. Galloway, Alan R. Townsend, Jan Willem Erisman, Mateete Bekunda, Zucong Cai, John R. Freney, Luiz A. Martinelli, Sybil P. Seitzinger, Mark A. Sutton, Transformation of the nitrogen cycle: recent trends, questions, and potential solutions, *Science* 320 (2008) 889–892.
- [36] G.-J. Lee, S. Anandan, S.J. Masten, J.J. Wu, Photocatalytic hydrogen evolution from water splitting using Cu doped ZnS microspheres under visible light irradiation, *Renew. Energy* 89 (2016) 18–26.
- [37] B. Zhang, J. Zhang, R. Duan, Q. Wan, X. Tan, Z. Su, B. Han, L. Zheng, G. Mo, BiOCl Nanosheets with Periodic Nanochannels for High-efficiency Photooxidation, *Nano Energy* 78 (2020), 105340.
- [38] J. Hao, S. Peng, H. Li, S. Dang, T. Qin, Y. Wen, J. Huang, F. Ma, D. Gao, F. Li, G. Cao, A low crystallinity oxygen-vacancy-rich Co<sub>3</sub>O<sub>4</sub> cathode for high-performance flexible asymmetric supercapacitors, *J. Mater. Chem. A* 6 (2018) 16094–16100.
- [39] X. Ren, M. Gao, Y. Zhang, Z. Zhang, X. Cao, B. Wang, X. Wang, Photocatalytic reduction of CO<sub>2</sub> on BiOX: Effect of halogen element type and surface oxygen vacancy mediated mechanism, *Appl. Catal. B-Environ.* 274 (2020), 119063.
- [40] X. Wang, G. Xu, Y. Tu, D. Wu, A. Li, X. Xie, BiOBr/PBCD-B-D dual-function catalyst with oxygen vacancies for Acid Orange 7 removal: evaluation of adsorption-photocatalysis performance and synergy mechanism, *Chem. Eng. J.* 411 (2021).
- [41] H. Wang, D. Yong, S. Chen, S. Jiang, X. Zhang, W. Shao, Q. Zhang, W. Yan, B. Pan, Y. Xie, Oxygen-vacancy-mediated exciton dissociation in BiOBr for boosting

- charge-carrier-involved molecular oxygen activation, *J. Am. Chem. Soc.* 140 (2018) 1760–1766.
- [42] S. Wang, X. Hai, X. Ding, K. Chang, Y. Xiang, X. Meng, Z. Yang, H. Chen, J. Ye, Light-switchable oxygen vacancies in ultrafine  $\text{Bi}_5\text{O}_7\text{Br}$  nanotubes for boosting solar-driven nitrogen fixation in pure water, *Adv. Mater.* 29 (2017) 1701774.
- [43] K. Chu, Y. Luo, P. Shen, X. Li, Q. Li, Y. Guo, Unveiling the synergy of O-vacancy and heterostructure over  $\text{MoO}_{3-x}/\text{MXene}$  for  $\text{N}_2$  electroreduction to  $\text{NH}_3$ , *Adv. Energy Mater.* 12 (2021) 2103022.
- [44] Y. Yang, D. Zhang, W. Ji, F. Bi, L. Song, X. Zhang, Uniform platinum nanoparticles loaded on Universitetet i Oslo-66 (UiO-66): Active and stable catalysts for gas toluene combustion, *J. Colloid Interface Sci.* 606 (2022) 1811–1822.
- [45] L. Zeng, L. Cui, C. Wang, W. Guo, C. Gong, In-situ modified the surface of Pt-doped perovskite catalyst for soot oxidation, *J. Hazard. Mater.* 383 (2020), 121210.
- [46] J.E. Mondloch, W. Bury, D. Fairén-Jiménez, S. Kwon, E.J. DeMarco, M.H. Weston, A.A. Sarjeant, S.T. Nguyen, P.C. Stair, R.Q. Snurr, O.K. Farha, J.T. Hupp, Vapor-phase metalation by atomic layer deposition in a metal-organic framework, *J. Am. Chem. Soc.* 135 (2013) 10294–10297.
- [47] D.V. Bavykin, A.A. Lapkin, P.K. Plucinski, L. Torrente-Murciano, J.M. Friedrich, F. C. Walsh, Deposition of Pt, Pd, Ru and Au on the surfaces of titanate nanotubes, *Top. Catal.* 39 (2006) 151–160.
- [48] Y. Bo, H. Wang, Y. Lin, T. Yang, R. Ye, Y. Li, C. Hu, P. Du, Y. Hu, Z. Liu, R. Long, C. Gao, B. Ye, L. Song, X. Wu, Y. Xiong, Altering hydrogenation pathways in photocatalytic nitrogen fixation by tuning local electronic structure of oxygen vacancy with dopant, *Angew. Chem. Int. Ed. Engl.* 60 (2021) 16085–16092.
- [49] H. Yin, Z. Chen, Y. Peng, S. Xiong, Y. Li, H. Yamashita, J. Li, Dual active centers bridged by oxygen vacancies of ruthenium single-atom hybrids supported on molybdenum oxide for photocatalytic ammonia synthesis, *Angew. Chem. Int. Ed. Engl.* 61 (2022) e202114242.
- [50] Q. Han, C. Wu, H. Jiao, R. Xu, Y. Wang, J. Xie, Q. Guo, J. Tang, Rational design of high-concentration  $\text{Ti}^{3+}$  in porous carbon-doped  $\text{TiO}_2$  nanosheets for efficient photocatalytic ammonia synthesis, *Adv. Mater.* 33 (2021), e2008180.
- [51] Z. Wang, J. Zhu, X. Zu, Y. Wu, S. Shang, P. Ling, P. Qiao, C. Liu, J. Hu, Y. Pan, J. Zhu, Y. Sun, Y. Xie, Selective  $\text{CO}_2$  photoreduction to  $\text{CH}_4$  via  $\text{Pd}^{\delta+}$ -assisted hydrodeoxygenation over  $\text{CeO}_2$  nanosheets, *Angew. Chem. Int. Ed. Engl.* 61 (2022), e202203249.
- [52] J. HRNDI, J. Xia, M.F. Chisholm, J. Zhong, C. Chen, X. Cao, F. Dong, Z. Chi, H. Chen, Y.X. Weng, J. Xiong, S.Z. Yang, H. Li, Z. Liu, S. Dai, Defect-tailoring mediated electron-hole separation in single-unit-cell  $\text{Bi}_5\text{O}_4\text{Br}$  nanosheets for boosting photocatalytic hydrogen evolution and nitrogen fixation, *Adv. Mater.* 31 (2019), e1807576.
- [53] X. Jiao, Z. Chen, X. Li, Y. Sun, S. Gao, W. Yan, C. Wang, Q. Zhang, Y. Lin, Y. Luo, Y. Xie, Defect-mediated electron-hole separation in one-unit-cell  $\text{ZnIn}_2\text{S}_4$  layers for boosted solar-driven  $\text{CO}_2$  reduction, *J. Am. Chem. Soc.* 139 (2017) 7586–7594.
- [54] Y. Han, D. Yue, M. Kan, Y. Wu, J. Zeng, Z. Bian, Y. Zhao, X. Qian,  $[\text{Mo}_3\text{S}_{13}]^{2-}$  modified  $\text{TiO}_2$  coating on non-woven fabric for efficient photocatalytic mineralization of acetone, *Appl. Catal. B-Environ.* 245 (2019) 190–196.
- [55] F. Lü, S. Zhao, R. Guo, J. He, X. Peng, H. Bao, J. Fu, L. Han, G. Qi, J. Luo, X. Tang, X. Liu, Nitrogen-coordinated single Fe sites for efficient electrocatalytic  $\text{N}_2$  fixation in neutral media, *Nano Energy* 61 (2019) 420–427.
- [56] Y. Wen, Z. Zhuang, H. Zhu, J. Hao, K. Chu, F. Lai, W. Zong, C. Wang, P. Ma, W. Dong, S. Lu, T. Liu, M. Du, Isolation of metalloid boron atoms in intermetallic carbide boosts the catalytic selectivity for electrocatalytic  $\text{N}_2$  fixation, *Adv. Energy Mater.* 11 (2021) 2102138.